



ELSEVIER

Available online at www.sciencedirect.com

ScienceDirect

www.elsevier.com/locate/jes**JES**
JOURNAL OF
ENVIRONMENTAL
SCIENCES
www.jesc.ac.cn

Meteorological mechanism for a large-scale persistent severe ozone pollution event over eastern China in 2017

Q4

Q3 Jia Mao^{1,2}, Lili Wang^{2,*}, Chuhan Lu^{1,**}, Jingda Liu^{1,2}, Mingge Li^{2,4}, Guiqian Tang², Dongsheng Ji², Nan Zhang⁵, Yuesi Wang^{2,3,4}

¹ Key Laboratory of Meteorological Disaster, Ministry of Education/Joint International Research Laboratory of Climate and Environment Change/Collaborative Innovation Center on Forecast and Evaluation of Meteorological Disasters, Nanjing University of Information Science and Technology, Nanjing, 210044, China

² State Key Laboratory of Atmospheric Boundary Layer Physics and Atmospheric Chemistry (LAPC), Institute of Atmospheric Physics, Chinese Academy of Sciences, Beijing, 100029, China

³ Center for Excellence in Regional Atmospheric Environment, Institute of Urban Environment, Chinese Academy of Sciences, Xiamen, 361021, China

⁴ University of Chinese Academy of Sciences, Beijing, 100049, China

⁵ Hebei Province Meteorological Observatory, Shijiazhuang, 050022, China

ARTICLE INFO

Article history:

Received 14 October 2019

Received in revised form

13 February 2020

Accepted 15 February 2020

Available online xxx

Keywords:

Surface ozone

Beijing-Tianjin-Hebei and

surrounding area

Synoptic patterns

Western Pacific subtropical high

Meteorological conditions

Inversion layer

ABSTRACT

An intensive and persistent regional ozone pollution event occurred over eastern China from 25 June to 5 July 2017. 73 out of 96 selected cities, most located in the Beijing-Tianjin-Hebei and the surrounding area (BTHS), suffered severe ozone pollution. A north-south contrast ozone distribution, with higher ozone ($199 \pm 33 \mu\text{g}/\text{m}^3$) in the BTHS and lower ozone ($118 \pm 25 \mu\text{g}/\text{m}^3$) in the Yangtze River Delta (YRD), was found to be dominated by the position of the West Pacific Subtropical High (WPSH) and mid-high latitude wave activities. In the BTHS, the positive anomalies of geopotential height at 500 hPa and temperature at the surface indicated favorable meteorological conditions for local ozone formation. Prevailing northwesterly winds in the mid-high troposphere and warm advection induced by weak southerly winds in the low troposphere resulted in low-moderate relative humidity (RH), less total cloud cover (TCC), strong solar radiation and high temperatures. Moreover, southerly winds prevailing over the BTHS aggravated the pollution due to regional transportation of O_3 and its precursors. On one hand, the deep sinking motion and inversion layer suppressed the dispersion of pollutants. On the other hand, O_3 -rich air in the upper layer was maintained at night due to temperature inversion, which facilitated O_3 vertical transport to the surface in the next-day morning due to elevated convection. Generally, temperature, UV radiation, and RH showed good correlations with O_3 in the BTHS, with rates of $8.51 (\mu\text{g}/\text{m}^3)/^\circ\text{C}$ (within the temperature range of $20\text{--}38^\circ\text{C}$), $59.54 (\mu\text{g}/\text{m}^3)/(\text{MJ}/\text{m}^2)$ and $-1.93 (\mu\text{g}/\text{m}^3)/\%$, respectively.

* Corresponding author.

** Corresponding author.

E-mail addresses: wll@mail.iap.ac.cn (L. Wang), luchuhan@nuist.edu.cn (C. Lu).

<https://doi.org/10.1016/j.jes.2020.02.019>

1001-0742/© 2020 The Research Center for Eco-Environmental Sciences, Chinese Academy of Sciences. Published by Elsevier B.V.

Introduction

Surface ozone is known as an important secondary air pollutant with potentially detrimental impacts on the environment and human health. Respiratory and cardiovascular mortality can be induced due to short-term exposure to high ambient ozone. Ozone is mainly formed via the photochemical reaction of volatile organic compounds (VOCs), carbon monoxide (CO), and nitrogen oxides ($\text{NO}_x = \text{NO} + \text{NO}_2$) in the presence of sunlight, specifically the UV spectrum (Xu et al., 2011; Wang et al., 2014; Li et al., 2018). Thus surface ozone, especially in urban areas, is usually influenced by anthropogenic emissions, and ozone concentration levels can be reduced by controlling its precursors (NOx and VOCs) to a certain extent (Tu et al., 2007; He et al., 2012; Wang et al., 2017; You et al., 2017).

The severity of O₃ pollution has been revealed to be not only strongly dependent on emissions and corresponding chemical reactions but also closely related to meteorological conditions (Fan et al., 2008; Pu et al., 2017; Zhao and Wang, 2017). High ozone pollution episodes are mainly dominated by high temperature, low total cloud cover, moderate relative humidity and low wind speed (He et al., 2012; Ding et al., 2013; Li et al., 2017; Pu et al., 2017). Since meteorological factors are dominated by synoptic-scale circulation patterns, extensive research has been conducted on the relationships between surface O₃ and synoptic systems (Liu et al., 2019). High ozone pollution usually occurs under the control of a high-pressure system in favor of relatively clear skies and strong solar radiation, which can result in an enhanced O₃ concentration through photochemical reactions (Pu et al., 2017; Li et al., 2019). Located before a low-pressure system or in front of a high-pressure system, where the prevailing wind favors pollutant transposition, the influenced region can also meet elevated ozone concentrations (Tang et al., 2010; Shen et al., 2015).

The WPSH plays an important role controlling the weather and climate over East China. Determined by the spatial patterns of diabatic heating, the migration of the WPSH always occurs in a stepwise fashion with two distinct northern jumps in mid-June and mid-July. The shift in the WPSH has a close relationship with East Asian monsoon and the rain belt over the Yangtze River Delta (YRD). Generally, the rain belt is located 8–10°N higher than the WPSH ridge, where the quasi-stationary front commonly stagnates at the sea surface layer. It has been revealed that WPSH is responsible for East Asian monsoon formation, precipitation over the YRD and air temperature and precipitation in North and South China (Zhang, 2001; Zhao and Wang, 2017). Zhao et al. analyzed the impact of WPSH intensity on surface ozone variability over eastern China based on empirical orthogonal function (EOF) analysis and found the variability in the WPSH is closely related to the meteorological conditions impacting ozone formation.

Over the past 5 years, stringent air pollution control strategies have mainly targeted fine particulate matter. In 2013, China issued the Air Pollution Prevention and Control Action Plan to reduce anthropogenic emissions (www.gov.cn/zwggk/2013-09/12/content_2486773.htm). Compared to the decreasing trend of PM_{2.5}, there is enough evidence indicating that eastern China, especially North China Plain (NCP) and YRD, has experienced severe O₃ pollution in recent years, especially in summer, due to rapid urbanization and industrialization (Cheng et al., 2018; Liu et al., 2019). Previous studies on meteorological mechanisms for ozone pollution have mainly examined the effects of meteorological factors on ozone at a single or several sites (Lin et al., 2008; Ding et al., 2013; Tan et al., 2018). In addition, most previous studies focused on the relations among daily or annual variations and ozone to those meteorological factors (Fan et al., 2008; Wang et al., 2008; Zhang et al., 2008; Wang et al., 2009; Xu et al., 2011; Ding et al., 2013). The evolution of a large-scale persistent regional ozone pollution episode has not been deeply explored due to the scarcity of O₃ datasets in China before 2013.

Regional meteorological conditions can significantly influence ozone production and distribution, the impacts of primary synoptic patterns on regional ozone characteristics should be studied in depth. However, insufficient research has been carried out to reveal the temporal and spatial evolution of ozone pollution on a large scale with observational data. During the summertime (June–July–August) from 2014 to 2017, ozone pollution episodes exceeding 10 days only occurred twice over Beijing–Tianjin–Hebei and surrounding area (BTHS) and YRD. These two episodes were 11–21 June 2017 and 25 June - 5 July 2017 (Fig. S1). Through collecting in situ O₃ data, ground-based meteorological data and reanalysis meteorological datasets, the regional evolution characteristics and the meteorological formation mechanism (synoptic circulation dynamics and local meteorological conditions, as well as atmospheric boundary layer structure) of a large-scale persistent O₃ pollution episode over 96 cities (485 sites) during 24 June to 6 July 2017 over eastern China have been investigated. The results of this study can be important in providing a scientific basis for predicting regional O₃ pollution and formulating air quality control strategies over eastern China.

1. Data and methods

1.1. Data source

Hourly surface ozone and PM_{2.5} concentrations from 24 June to 6 July 2017 were provided by the China National Environment Monitoring Center Network (<http://106.37.208.233:20035/>) established by the Ministry of Ecology and Environment of China. The original unit of ozone observations is $\mu\text{g}/\text{m}^3$, which can be converted to mixing ratios (units: ppbv) using a

constant (e.g., 0.5 at a temperature of 25°C and pressure of 1013.25 hPa). In this study, we still used the original unit for ozone. According to the technical regulation for ambient air quality assessment (HJ 663–2013, <http://www.mee.gov.cn/>), the maximum daily 8-h average surface ozone (MDA8 O₃) of a single station is defined with at least 14 valid hourly values from 8:00 to 24:00. The results are still valid if the MDA8 O₃ exceeds the national concentration limit standard (160 µg/m³) with less than 14 valid values. The ambient air quality assessment for an urban city is the corresponding average over all the sites within the city range. In this study, 96 urban cities (485 sites) were selected to reflect the regional ozone status of eastern China, covering provinces and cities including Beijing, Tianjin, Hebei, Shanxi, Henan, Shandong, Anhui, Jiangsu, Zhejiang, and Shanghai, which is usually regarded as one of the most densely populated areas in China as shown in Fig. 1b. The locations of these cities are shown in Fig. 1a and Table S1.

The daily observational meteorological data of each station were obtained from the China Meteorological Administration (CMA, <http://www.data.cma.cn/>), including wind speed, surface pressure and precipitation. Since MDA8 O₃ usually occurs in the afternoon due to intensive solar radiation, the temperature (Tem), relative humidity (RH) and total cloud cover (TCC) in the afternoon were averaged from two measurements (at local hours 14:00 and 17:00) per day from China Meteorological Administration in the Meteorological Information Combine Analysis and Process System (MICAPS). The meteorological data of each city were retrieved from the closest meteorological station. Sounding data were downloaded from the website (<http://www.weather.uwyo.edu/upperair/sounding.html>) in Beijing, Zhangqiu, Taiyuan and Zhengzhou (Fig. 1a).

Hourly reanalysis data including sea surface pressure, geopotential height, horizontal wind (U-wind and V-wind),

divergence, air temperature, downward UV radiation (UV) and planetary boundary layer height (PBLH) were provided by the fifth generation European Center for Medium-Range Weather Forecasts (ECMWF) reanalysis dataset (ERA5) at different vertical levels, with a spatial resolution of 0.5° × 0.5°. It should be noted that in section 2.2.2, we extract the nearest grid UV data for each city with a resolution of 0.25° × 0.25°.

1.2. Methods

To refine our understanding of O₃ evolution characteristics over eastern China, several different statistics were utilized. Factor analysis (FA) was applied to sort 96 cities into different categories (Sousa et al., 2007; Langford et al., 2009; Zheng et al., 2010). According to the ozone variability in each city during the selected pollution episode, cities with similar variations were considered as one category.

Pearson's paired correlation coefficient (R) was calculated to investigate the linear relationships among the cities in each category. The spatial coefficients of variation (CV) and the coefficients of divergence (COD) were calculated to analyze the spatial and temporal variations of the MDA8 ozone in each category (Cyrus et al., 2008; Krudyszka et al., 2008; Sarnat et al., 2010; Tang et al., 2012). The CV was defined as the mean of the standard deviation of the spatial distribution divided by the mean of the distributions and finally averaged over the sampling days. The COD was calculated according to the following:

$$COD_{fh} = \sqrt{\frac{1}{n} \sum_{i=1}^n \left(\frac{x_{if} - x_{ih}}{x_{if} + x_{ih}} \right)^2}$$

where x_{if} and x_{ih} represent the i -th concentration observed at the f -th and h -th sites, respectively, and n is the sampling size of the observations at each city. The COD of each category was calculated as the mean of the pair-wisely values. These two

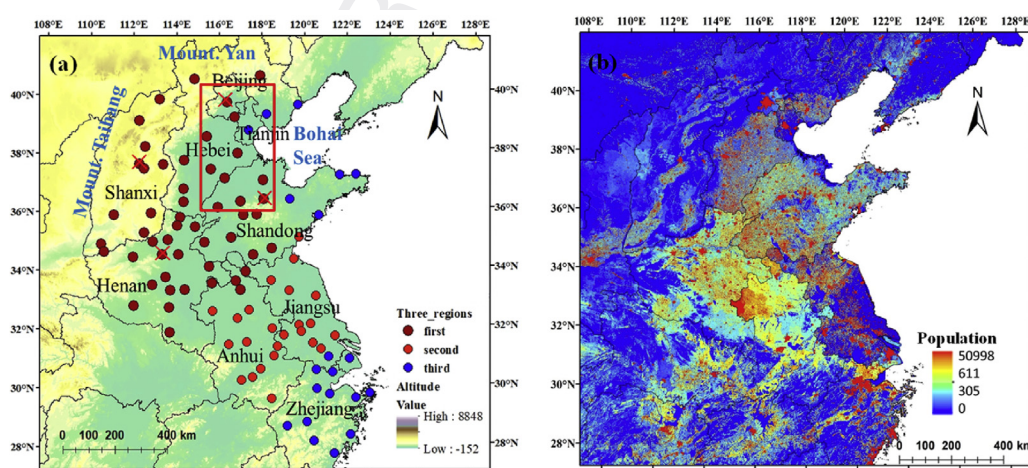


Fig. 1 – The topography and locations of the 96 urban cities (a) and population distribution (b) over eastern China. The selected cities are divided into three categories: the Beijing-Tianjin-Hebei and the surrounding area (BTHS), the northern (23 cities) areas of the Yangtze River Delta (YRDN) and the southern (21 cities) areas of the Yangtze River Delta (YRDS), marked by brown, red and blue dots, respectively. Red crosses represent cities with sounding meteorological data; the red rectangular box represents the core BTH area.

statistics can reflect the heterogeneity of sites in the same region to some extent. Low CV and COD values indicate a strong uniformity of the ozone characteristics in one category.

2. Results and discussion

2.1. Overview of regional ozone variability

Fig. 2 depicts the daily distribution of O_3 and $PM_{2.5}$ for 96 cities, with cities arranged by latitudes from north to south (from top to bottom). The legend represents the different air-quality levels for excellent (green), good (yellow), lightly polluted (orange), moderately polluted (red) and heavily polluted days (purple). It is obvious that the severe large-scale ozone pollution displayed a north-south contrast distribution. Cities located in the higher latitudes experienced more serious pollution, with the maximum value up to $314 \mu\text{g}/\text{m}^3$. Due to rigorous emission control regulations, the $PM_{2.5}$ concentrations of the 96 urban sites range from 10 to $99 \mu\text{g}/\text{m}^3$ (Fig. 2b) during the same period, which are lower than those during 2013–2015 (Wang et al., 2018). The decrease in $PM_{2.5}$ may result in intensified ozone pollution as it can facilitate the increase in UV radiation at the surface and slow down the sink of hydroperoxy radicals, thus speeding up ozone production (Li et al., 2018). Considering the north-south contrast in MDA8 O_3 variation and distribution over eastern China (Fig. 2a), FA was first applied to identify cities with homogeneous ozone variation trends. The classification standards are shown in Table S1. Three factors exhibited 31.8%, 25.4% and 17.6% of the variability in the total MDA8 O_3 concentrations; finally, three homogenous groups were identified (Fig. 1a). The first group included 52 cities located in the BTHS; the northern (23 cities) and southern (21 cities) areas of the Yangtze River Delta (YRD) were the second and third categories (including several

Table 1 – Intersite uniformity statistics of ozone for different regions.

Category	CV	COD
Category1 (BTHS)	18%	0.13
Category2 (YRDN)	25%	0.13
Category3 (YRDS)	29%	0.15

coastal cities over Shandong and Hebei), named YRDN and YRDS, respectively. The COD pairwise values of each ozone group were calculated to validate the rationality of the classification. A COD of 0.2 served as the threshold to identify the heterogeneity between two sites (Krudyszka et al., 2008). As shown in Table 1, MDA8 O_3 exhibited strong homogeneity among each group, with the CV and COD ranging from 18% to 29% and 0.07 to 0.15, respectively. The CV and COD were both the lowest in the BTHS, which experienced the most severe ozone pollution.

Fig. 3 and Table S1 show the temporal variation in and spatial distribution of the regional means and exceeding occurrences of MDA8 ozone in each city. Generally, cities in the BTHS experienced a more intensive and successive pollution period. On 25 June, 38 out of 52 cities exceeded the grade II national air quality standard ($160 \mu\text{g}/\text{m}^3$), and the regional mean ozone concentration was up to $182 \pm 30 \mu\text{g}/\text{m}^3$. In the next few days, ozone pollution was further intensified regardless of the scope and intensity. The maximum regional mean ozone concentration up to $221 \pm 32 \mu\text{g}/\text{m}^3$ occurred on 27 June, and over 98% of the cities suffered heavy ozone pollution. The ozone concentration began to decrease after 3 July and reached its minimum value on 6 July at $89 \pm 28 \mu\text{g}/\text{m}^3$, indicating the end of this pollution event. During the pollution process, 51 out of 52 cities in the BTHS were exposed to ozone pollution, with the regional daily mean concentration and

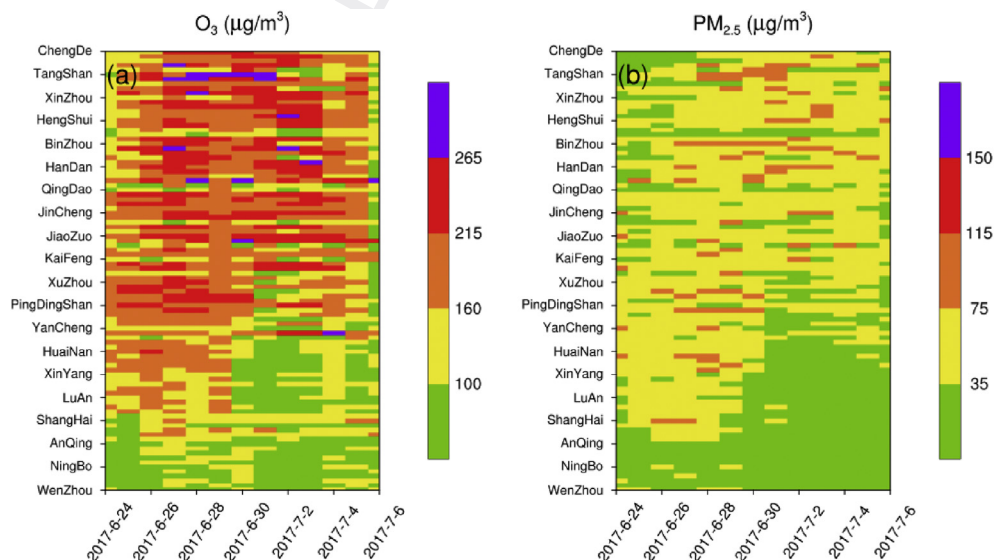


Fig. 2 – Time series of the maximum daily 8-h average surface ozone (MDA8 O_3) (a) and $PM_{2.5}$ (b) concentrations for 96 cities from 24 June to 6 July. Cities are arranged by latitude from north to south; the legend represents the different air-quality levels for excellent (green), good (yellow), lightly polluted (orange), moderately polluted (red) and heavily polluted days (purple) with cut off concentrations of 100, 160, 215, 265 $\mu\text{g}/\text{m}^3$.

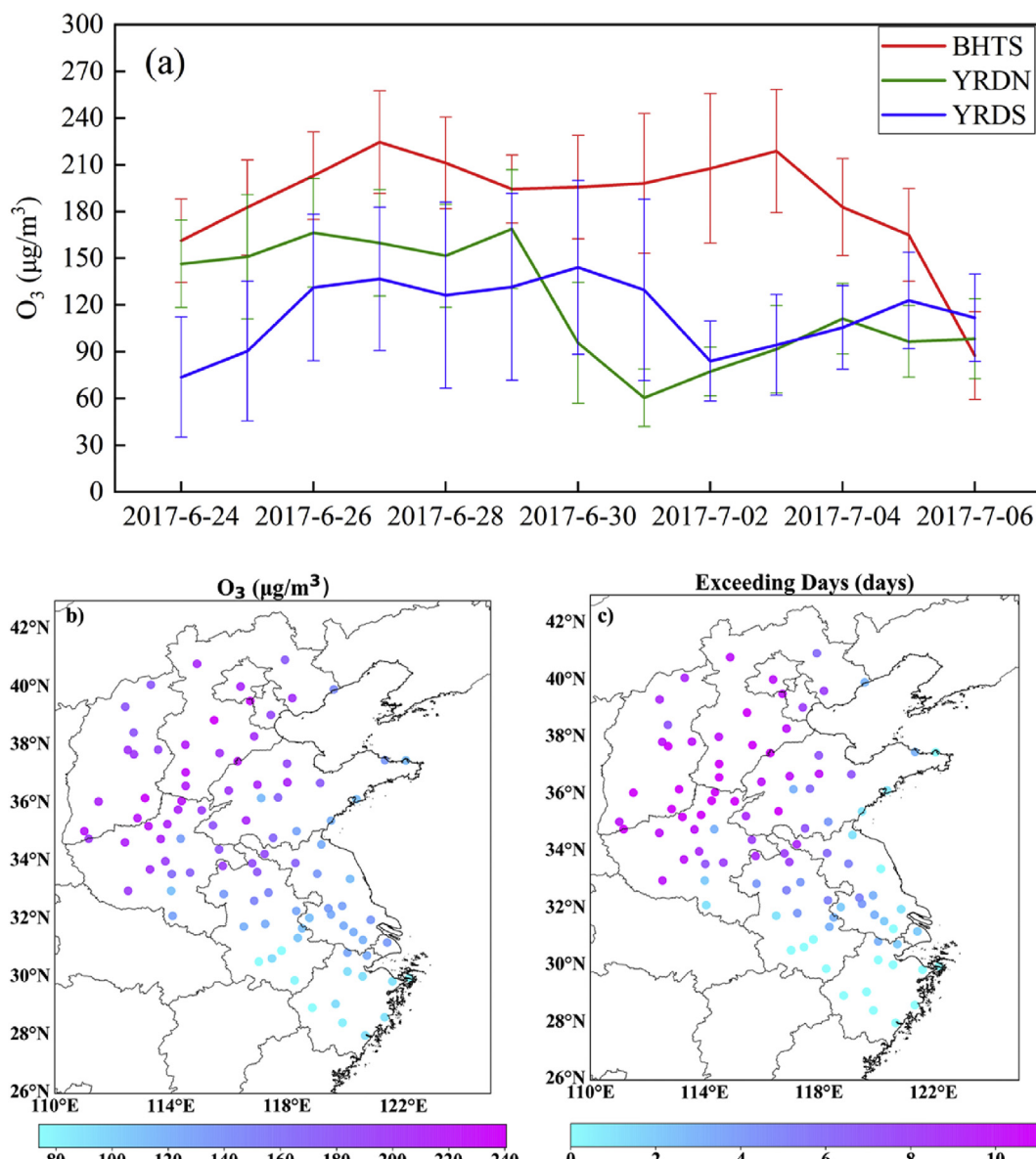


Fig. 3 – Time series of regional averaged MDA8 ozone concentration over each region (a) from 24 June to 6 July; spatial distribution of mean MDA8 ozone (b) and the number of ozone pollution days (c) during the pollution event from 25 June to 5 July.

averaged exceedance being $199 \pm 33 \mu\text{g}/\text{m}^3$ and 9.3 days, respectively. In contrast, cities located in the YRD experienced relatively weak pollution. The regional ozone concentration of the YRDN ranged from 140 to $160 \mu\text{g}/\text{m}^3$ from 25 to 29 June, followed by a sudden drop on 30 June at $94 \pm 38 \mu\text{g}/\text{m}^3$. The maximum regional ozone concentration of the YRDS reached $144 \pm 56 \mu\text{g}/\text{m}^3$, and the ozone concentration gradually increased after 2 July. The domain-averaged MDA8 ozone concentrations in the YRDN and YRDS were $119 \pm 38 \mu\text{g}/\text{m}^3$ and $117 \pm 20 \mu\text{g}/\text{m}^3$, respectively. The averaged exceedances of YRDN and YRDS were 2.7 and 1.9 days, respectively.

Ozone concentrations have been determined by a combination of precursor emissions and meteorological conditions. To investigate whether the variability in ozone precursors or meteorological conditions mainly contributed to the severe

regional ozone pollution in the BTHS (the most polluted region), Pearson's paired correlation coefficient (R), CV and COD are shown in Table 2. Due to the lack of VOC observations, CO was used to reflect the VOC concentration because it has a high correlation with VOC. The intersite correlation for MDA8 ozone was the strongest at 0.67, compared to 0.05 and 0.27 for

Table 2 – Intersite uniformity statistics for cities in the BTHS.

Pollutants	R	CV	COD
O ₃	0.64	18%	0.13
CO	0.04	52%	0.21
NO ₂	0.29	32%	0.19

CO and NO₂, respectively. MDA8 ozone also exhibited the least variability, with mean CV and intersite mean COD values of 18% and 0.13 respectively, indicating homogenous ozone variability among each city. However, the CVs of NO₂ and CO were 31% and 48%, respectively. The CODs for NO₂ and CO were 0.19–0.21, showing the heterogeneous variability in ozone precursors. The homogeneity of ozone and the heterogeneity of NO₂ and CO among the sites in the BTHS indicated that the response of O₃ to precursors was highly nonlinear (Tang et al., 2012; Wang et al., 2013; You et al., 2017), and the precursor concentrations could not determine the variation trends of O₃.

The basic cause of O₃ formation is excessive precursor emissions (e.g., VOCs and NO_x), and a chemistry-intensive method is usually used for estimating the effects of VOCs and NO_x emission changes on peak O₃ (Seinfeld, 1988), which is named as the empirical kinetic modeling approach (EKMA). The EKMA curve can vary greatly at different sites under different weather conditions, which revealed the response of O₃ to precursors was highly nonlinear. In addition, previous studies have indicated that the formation of severe O₃ pollution was characterized by a complex interplay among net chemical production, horizontal advection and vertical turbulence, dry deposition and diffusion processes (Gong and Liao, 2019). In particular, chemical reactions can be influenced by meteorological conditions, e.g., high temperature and solar radiation, as well as more stagnant atmospheric conditions (Pu et al., 2017). Thus, in addition to the emission of ozone precursors, meteorological conditions also play a key role in the formation of O₃ events. The photochemical production, horizontal and vertical transportation, and diffusion processes of O₃ are closely related to meteorological conditions (Wang et al., 2017; Gong and Liao, 2019). The meteorological fields (such as temperature and relative humidity) were found to have a significant linear relationship with O₃ at both one-site and regional scales (He et al., 2012; Li et al., 2018; Wang et al., 2018). In this study, similar variation trends of O₃ among different cities were observed in both the BTHS and the YRD regions (Section 2.3). Consequently, we focus on the similar variabilities among different cities in this long-lasting large-scale O₃ event. Since the precursor concentration variations did not determine the variation trends of O₃, the meteorological conditions were the primary reasons for the homogeneous variations in O₃ over the BTHS and the YRD (He et al., 2012; Li et al., 2018; Wang et al., 2018). In the following section, we will investigate the influencing synoptic patterns and meteorological conditions accounting for the O₃ characteristics in different regions.

2.2. The effects of circulation patterns on regional ozone pollution

2.2.1. The movements of the WPSH

Meiyu is an important climate phenomenon characterized by persistent rainfall over the YRD from June to July, which is also called Changma in the Korean Peninsula and Baiu in mid and south Japan (Ge et al., 2008). The rain belt over the YRD is usually related to the location of the WPSH. Fig. 4 shows the location of WPSH and the corresponding ridge line during the pollution process. In this context, the WPSH ridge was defined

as the line within the range of 5880 gpm where $u = 0$ and $du/dy > 0$. From 24 to 29 June, with the ridge line maintained at approximately 22°N, the YRDS was generally located on the north side of the subtropical high, which is the water vapor passage. At the surface pressure field, the YRDS was disturbed by the quasi-stationary front on 24 and 25 June (not shown), which provided instability for rainfall. In the following four days from 30 June to 2 July, the WPSH moved east out of the inland. On 3 July, the WPSH extended to the inland anew and jumped northward with the ridge line staying at 25°N, and the YRDS was basically under the control of the WPSH.

The western and northern boundaries of the WPSH are always closely related to the water vapor passage. High RH favors increased TCC, which can further influence other meteorological factors, such as solar radiation. With the northward movement of the WPSH from 22 to 25°N, the maximum value of the RH also moved northward from the YRDS to the YRDN, which accounts for the ozone variability over YRD region. In section 2.3.1, we will discuss what impacts the step-fashion movement of WPSH brought on the meteorological conditions over YRD region.

2.2.2. Synoptic circulations over the BTHS

In addition to the WPSH, mid-high latitude wave activities are also closely related to the meteorological conditions over the BTHS (Xu et al., 2019). During the pollution period, the BTHS was under the control of the positive geopotential height anomaly center at 500 hPa (Fig. S2), which is often closely related to stable weather conditions over BTHS (Zhong et al., 2019). Thus the mid-high latitude circulation patterns will be further discussed to investigate their impacts on the meteorological conditions over the BTHS.

Fig. 5 depicts the sea-level pressure field, geopotential height, horizontal wind fields and air temperature distribution at multiple levels. At the beginning of the regional ozone pollution episode, the BTHS was in front of the high-pressure system, where dry clean northwesterly winds prevailed at 500 and 200 hPa. The dry air from higher latitudes favors a low relative humidity and less cloud cover, allowing more solar radiation to reach the ground and higher temperature. Moreover, the high-pressure ridge at 500 and 200 hPa can impede the northward movement of the WPSH, inhibiting the transportation of water vapor from the low latitudes. At sea-level pressure, the BTHS was under the control of a local high-pressure system on 25 and 26 June, and the O₃ concentration began to increase under stable weather conditions with downward motion (Fig. 6) and little cloud cover (Fig. S3). On 27 June, the BTHS was at the front of the shallow warm low-pressure system, the center of which was located in the Mongolia. Warm advection due to southerly winds prevailing in the lower troposphere (e.g., surface and 850 hPa layers) can bring pollutants to BTHS (Zhu and Liang, 2012; Whaley et al., 2015). Before large-scale O₃ pollution occurred over the BTHS, O₃ and its precursor concentrations in the southern BTHS were high on 24 June. However, during the pollution process, O₃ and its precursor concentrations gradually increased over the northern BTHS (Figs. S4, S5, S6). When the episode ended, O₃ concentrations pronouncedly decreased in the southern domain and increased in the northern BTHS. The results indicate that the regional transport caused by the

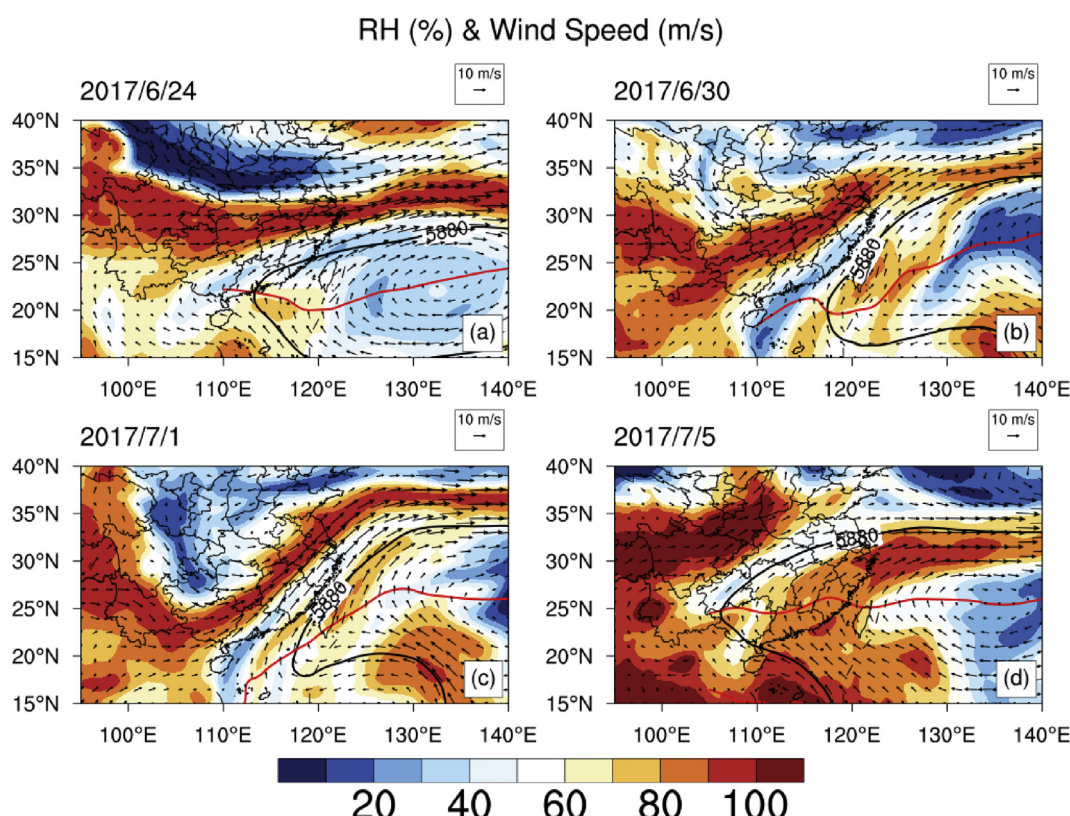


Fig. 4 – Distribution of horizontal wind at 500 hPa (vector), the position of the West Pacific Subtropical High (WPSH) ridge line (red line), 5880 gpm line (dark line) and relative humidity (RH) (shaded) on 24 June (a), 30 June (b), 1 July (c) and 5 July (d).

southerly winds strengthened O_3 pollution, which is consistent with the findings in previous studies (Gong and Liao, 2019; Liu et al., 2019). From 27 June to 3 July, similar vertical atmospheric circulation pattern controlled BTHS. As the influencing warm ridge continuously moved eastward, the BTHS was then at the back of the ridge, and the dominant wind gradually shifted to the south on 4 July (Fig. S7). The wind shift favored the further northward movement of the WPSH, which brought water vapor to the BTHS. On 6 July, a strong cold front came into the BTHS (not shown), facilitating the thorough dispersion of pollutants and ozone declined quickly.

2.3. Influence of meteorological factors on regional ozone pollution

2.3.1. Evolution of meteorological factors during regional ozone pollution episodes

Relative humidity, temperature and solar radiation are all essential for the chemical reactions involved ozone production. Solar radiation can promote NO_2 photolysis, which is an important pathway for ozone formation ($NO_2 + hv + O_2 \rightarrow O_3 + NO$) (Tan et al., 2018). Temperature can not only increase the photolysis reaction rates but also influence the rate constant of all the precursors. Water vapor also plays an important role in the photochemical reaction due to the generated OH ($O(^1D) + H_2O \rightarrow 2OH$) (Xu et al., 2011; Pu et al., 2017; Zhao et al., 2019).

The ozone concentration over the BTHS remained high throughout the pollution process. Higher temperature, moderate humidity, less total cloud cover, and stronger downward UV radiation in BTHS were responsible for the surface ozone production. After 3 July, with the northward movement of WPSH and the influence of the trough, precipitation occurred in the BTHS, resulting in increased RH and decreased temperature (Figs. 4, 5), and ozone concentration declined (Fig. 3a). Consistent with the ozone variation trend, the meteorological conditions in the YRDN also come into two stages. In contrast to the second stage (30 June - 5 July), the YRDN had a lower TCC and RH and higher Tem and UV in the first stage (25–29 June). The RH then increased to 92.9% due to the movement of the WPSH, contributing to the continuous precipitation from 29 June. In YRDS, the ozone concentration remained low, although the temperature increased after 28 June due to continuous rainfall. On one hand, precipitation over the BTHS can scavenge soluble precursors, such as NO_2 ; on the other hand, the increased TCC and RH, decreased temperature and UV virtually hinder ozone photochemical reactions.

2.3.2. Dependence of ozone on temperature, UV radiation, and relative humidity

From the discussion above, stronger radiation, high temperature and moderate humidity have been shown to be important for elevated O_3 concentrations. To quantify the relationship between O_3 concentration and meteorological

HGT (gpm) & Wind Speed (m/s) & Tem (K)

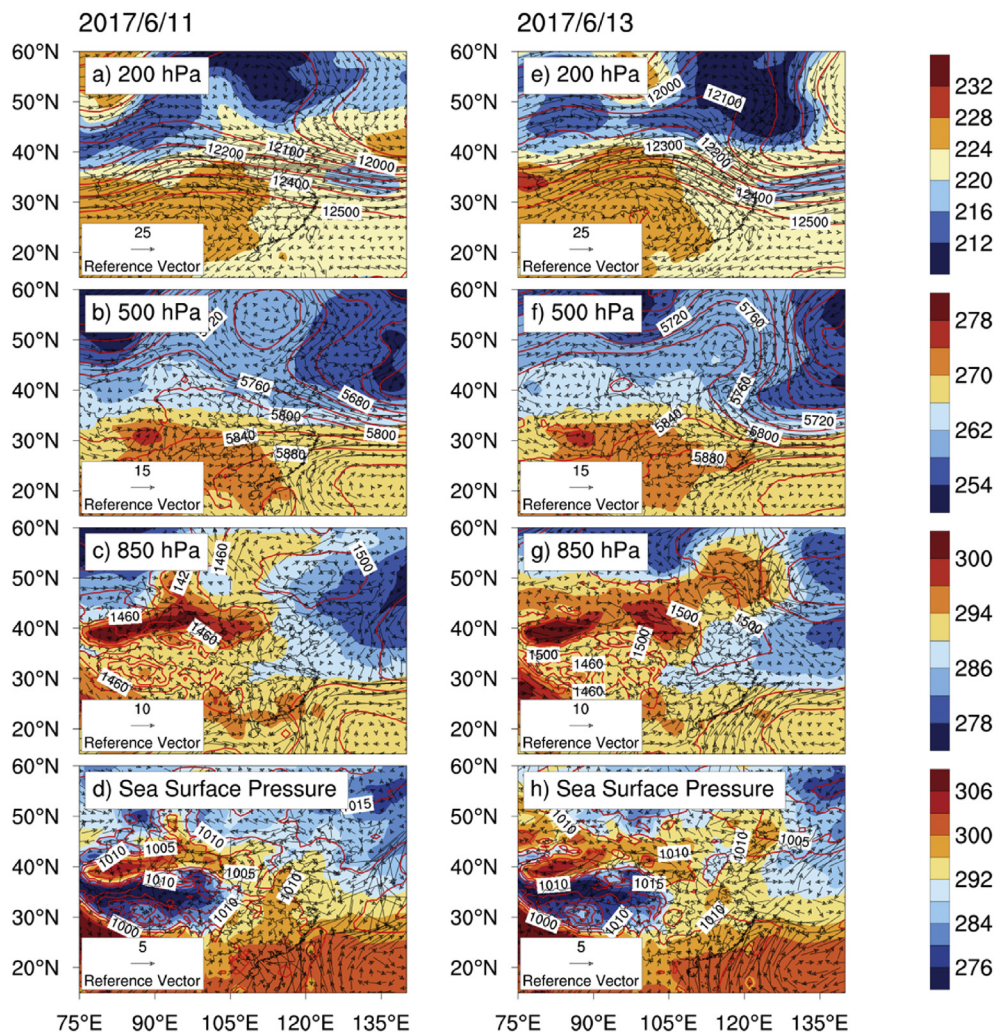


Fig. 5 – Distribution of geopotential height field (HGT; red contours) at 200, 500 and 850 hPa; sea-level pressure field; horizontal wind (200, 500 and 850 hPa and 10 m; vector) and air temperature (Tem; 200, 500 and 850 hPa and 2 m; shaded) at 14:00 local time (LT) on 25 June (from (a) to (d)) and 27 June (from (e) to (h)).

factors, the dependence of ozone on Tem, UV radiation, and RH are further analyzed in different regions.

Previous studies have revealed that O_3 is positively correlated with Tem, which is consistent with the results depicted in Fig. 7a and d. The Pearson's correlation coefficient (R) for the BTHS was 0.91; no significant correlations were found in the YRD area. Compared to Tem, UV seemed to have a more significant correlation with O_3 concentration in each region, with R values of 0.95, 0.67 and 0.54 in the BTHS, YRDN and YRD, respectively (Fig. 7b). This is likely because temperature influences photochemical reaction rates, while UV radiation is the main driver of photochemical reactions (Xu et al., 2011). In addition, during this regional ozone episode, high temperature is not always related to high UV radiation (Fig. S8). Strong negative correlations between RH and ozone concentration were commonly found in the BTHS, YRDN and YRDS (Fig. 7c). The R and slope values in the BTHS, YRDN and YRDS are

−0.92, −0.88, and −0.63 and 2.21, 3.62, and 2.67 ($\mu\text{g}/\text{m}^3$)/%, respectively.

It should be noted that temperature, UV radiation and RH all had a more significant correlation with O_3 concentration over the BTHS, in which ozone pollution was more intensive. The relationships among O_3 and influencing meteorological factors over the BTHS were further investigated based on the daily values for all cities. Temperature, UV radiation, and RH showed good correlations with O_3 in the BTHS, with R values of 0.63, 0.73 and −0.7, respectively. The slopes of temperature, UV and RH were 8.51 ($\mu\text{g}/\text{m}^3$)/ $^{\circ}\text{C}$, 59.54 ($\mu\text{g}/\text{m}^3$)/(MJ/ m^2) and −1.93 ($\mu\text{g}/\text{m}^3$)/%, respectively. For UV radiation greater than 2 MJ/ m^2 , O_3 concentrations increased more significantly with a slope of 72.36 ($\mu\text{g}/\text{m}^3$)/(MJ/ m^2). The increased slope for UV radiation indicated that O_3 concentrations may be more sensitive to UV variation under a threshold value.

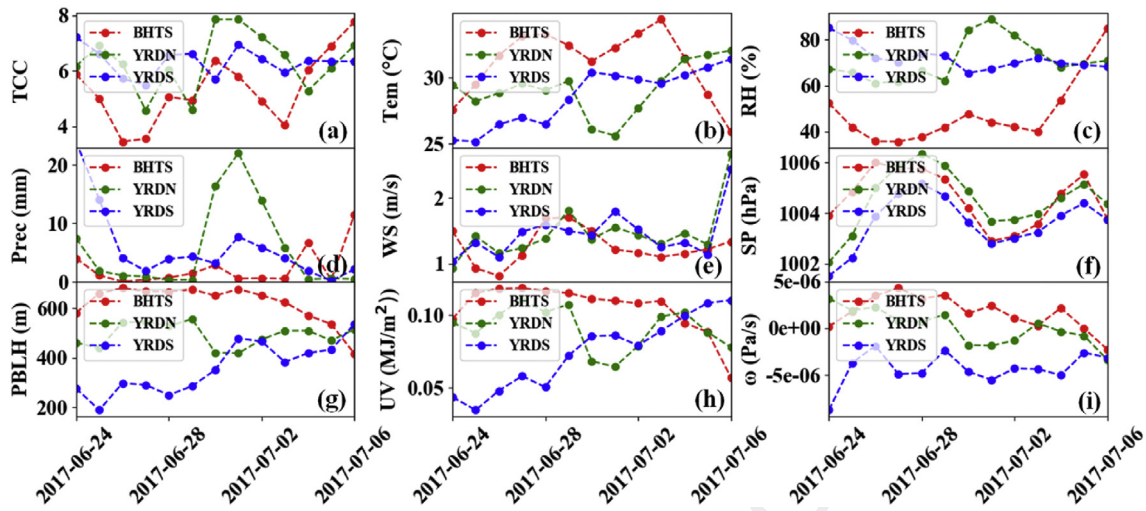


Fig. 6 – Time series of meteorological conditions over each region: total cloud cover (TCC), temperature (Tem) and relative humidity (RH) in the afternoon from (a) to (c). Daily means for precipitation (Prec), wind speed (WS), sea-level pressure (SP), planetary boundary layer height (PBLH), downward UV radiation (UV) at the surface, and vertical velocity (ω) at 850 hPa from (d) to (i).

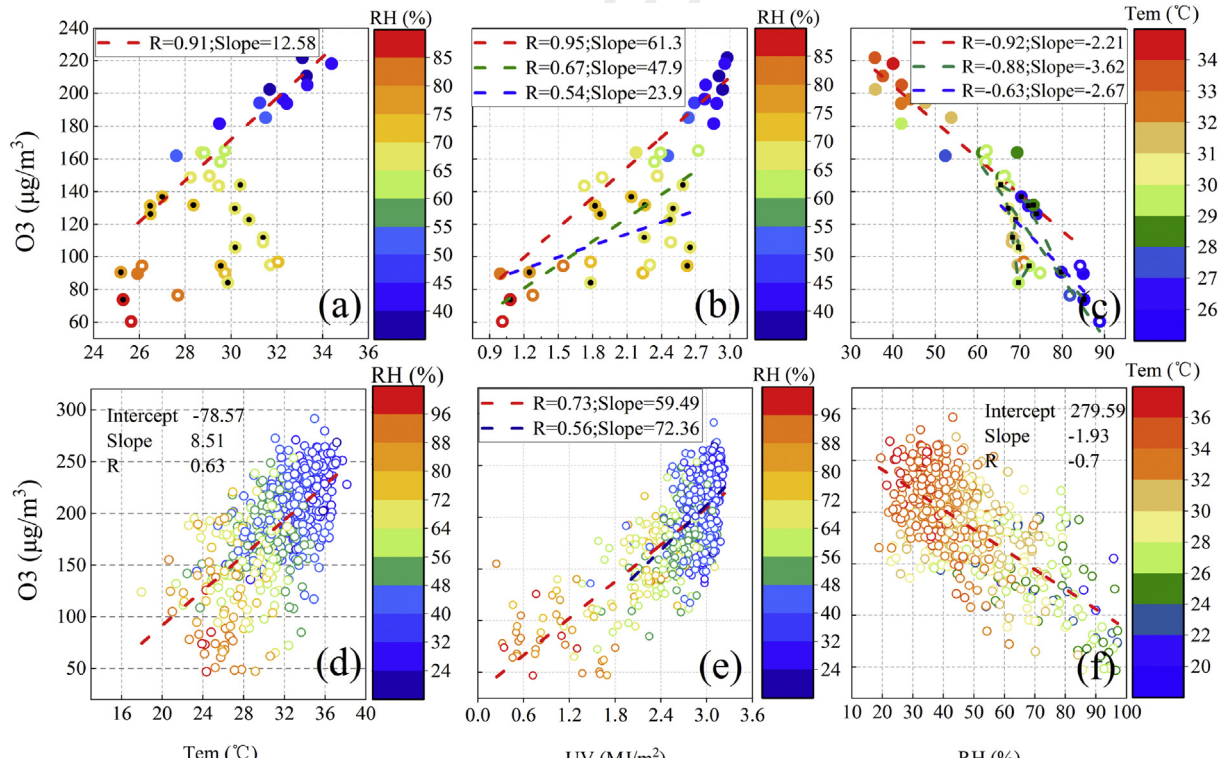


Fig. 7 – Scatter plots between regional mean MDA8 O_3 and temperature (Tem) (a), UV radiation (UV) (b) and relative humidity (RH) (c). The linear fitting lines of the BHTS, YRDN, and YRDS are red, green and blue; solid dots without and with white and black dots represent the BHTS, YRDN and YRDS, respectively. Scatter plots between daily MDA8 O_3 and Tem (d), UV (e) and RH (f) for all cities in the BHTS. The red lines represent the linear fitting lines and the blue line represents the fitting at $UV > 2 \cdot 10^6 \text{ J/m}^2$ (2 MJ/m^2). R represents Pearson's correlation coefficient.

3. Dynamic mechanism

In addition to chemical formation and horizontal transportation, vertical motion is also a significant dynamic factor in ozone concentration as it has a considerable effect on the vertical dispersion of pollutants (Shi et al., 2018). Fig. 8 shows the composite pressure-latitude profiles of the temperature anomaly, wind divergence and vertical velocity averaged from 36° to 41°N (Fig. 8 a, b and c). The wind displayed a convergence-divergence-convergence structure: a shallow convergence at 1000-900 hPa, followed by a divergence at 900-800 hPa, and a convergence at 800-600 hPa. This vertical structure favors ozone-benefiting sinking motion according to the continuous theorem of quality (Wu et al., 2017). The core BTH region (marked by the red rectangle in Fig. 1) was completely dominated by deep sinking motion from 1000 to 500 hPa. Next, the daily vertical distributions of temperature, wind divergence and vertical velocity anomaly are shown in Fig. 8 d, e and f. The temperature, wind divergence and vertical velocity showed the abovementioned distribution during the pollution event. The deep sinking motion from 1000 to 500 hPa can restrain the dispersion of pollutants within a lower layer.

Fig. 9 shows the hourly vertical profiles of temperature in Beijing based on ERA5 data, and Fig. S9 shows temperature profiles at Beijing, Taiyuan, Zhengzhou and Zhangqiu at 8:00 and 20:00 local time (LT) based on in situ sounding data. It was observed that temperatures pronouncedly decreased with height at midday in Beijing, while the vertical lapse rate of temperatures notably diminished at night and early morning accompanied by inversions. Temperature inversions can cut off the mass exchange between the upper and lower layers

(Fan et al., 2008). Under this situation, a large amount of NO emissions at night can only titrate ozone at the surface (NO-rich layer), and the ozone generated through photochemical reactions in the daytime can be preserved in the upper layer at night due to inversion. The vertical distribution of O₃ revealed that a higher level of O₃ was produced in the boundary layer in the daytime and corresponded to higher O₃ concentrations in the upper layer that occurred on the following night (Yan et al., 2018; Farris et al., 2019; Zhao et al., 2019). Under this situation, once the thermal inversion layer is broken as the sun rises (Figs. 9 and S9), O₃ in the upper layer (ozone-rich layer in the night due to the lack of NO titration) can be transported to the ground with the sinking motion (Zhao et al., 2019).

Consequently, the favorable meteorological conditions, sinking motion and temperature inversion jointly determined the heavy and persistent ozone pollution over the BTHS. A schematic representation of the meteorological formation mechanism for persistent regional ozone pollution over the BTHS is shown in Fig. 10. Located in front of a ridge, the BTHS was dominated by the dry northwesterly wind in the middle and upper troposphere, which resulted in stable weather conditions with low-moderate humidity, less cloud cover, and higher solar radiation and temperature in the BTHS. Weak southerly winds in front of the shallow warm low-pressure system in the low troposphere favored the accumulation of pollutants, as southerly winds conveyed the aged air mass from the south to the BTHS. A deep sinking motion and inversion layer suppressed the vertical dispersion of pollutants. Additionally, the inversion layer in the lower troposphere facilitated O₃ vertical transport from upper boundary layer to the surface. If the abovementioned conditions remain

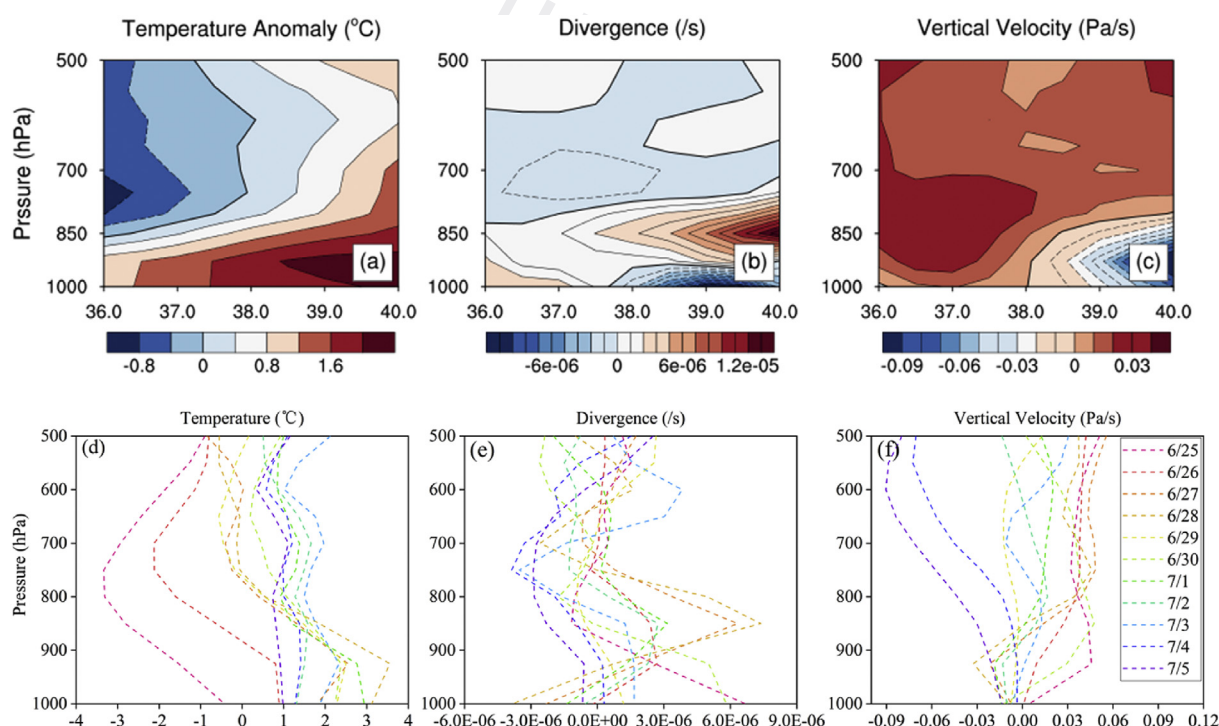


Fig. 8 – Composite pressure-latitude profiles of temperature anomaly (a), wind divergence (b) and vertical velocity (c) averaged between 116 and 119°N from 25 June to 5 July; vertical distribution of temperature (d), wind divergence (e) and vertical velocity (f) anomaly of the pollution event from 25 June to 5 July.

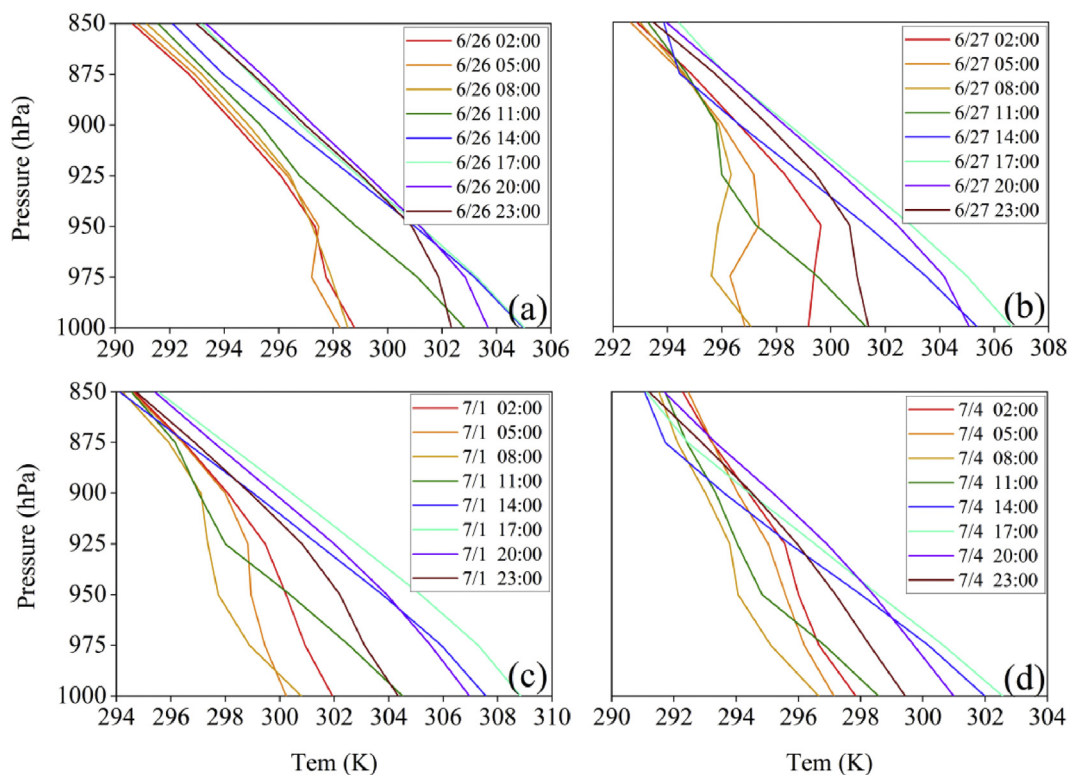


Fig. 9 – Daily vertical profiles of temperatures in Beijing on 26 June (a), 27 June (b), 1 July (c) and 4 (d) July. Hourly temperature data were retrieved at the nearest grid from Beijing.

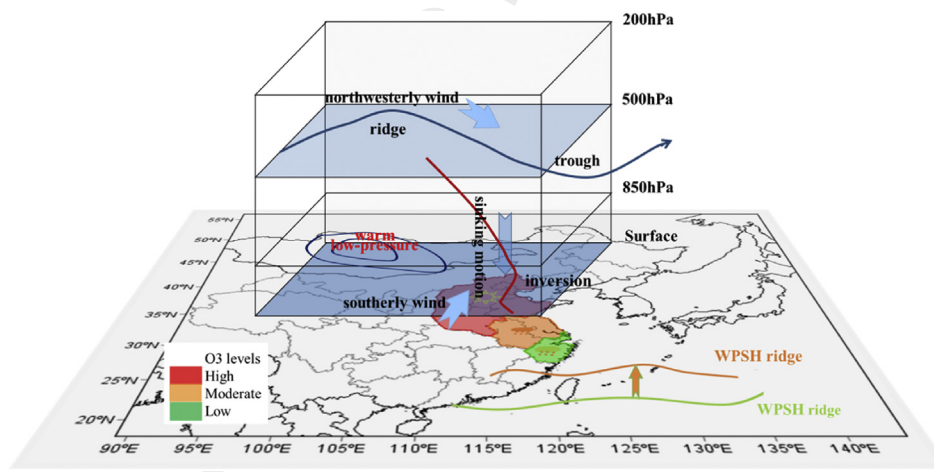


Fig. 10 – Schematic representation of the meteorological formation mechanism for the persistent regional ozone pollution over the BTHS and YRD. The initial and final locations of the WPSH ridge line during the pollution process are marked by green and yellow, respectively.

in the BTHS for a long time, the ozone event will be continuously maintained and further exacerbated.

4. Conclusions

In this study, an 11-day regional ozone pollution event in the summer of 2017 was investigated based on in situ observation data for 96 cities over eastern China. Seventy-three cities

mainly located in the BTHS experienced ozone pollution with maximum ozone concentrations up to $314 \mu\text{g}/\text{m}^3$, indicating the large scope and intensity of this pollution event. The impact of the meteorological dynamic mechanism on ozone was analyzed.

The movement of the WPSH (ridge sustained at $20\text{--}26^\circ\text{N}$) played an important role in the spatial distribution of ozone over the YRD region, which attributed to amounts of precipitation and insufficient radiation. The persistent high RH did

not favor ozone formation, thus leading to the relatively low ozone concentration over the YRD. Under the control of the anomalous high-pressure system in middle and upper troposphere, the BTHS was dominated by meteorological conditions favorable for ozone formation (Xu et al., 2019). Warm advection induced by southerly winds was prevalent in the low troposphere over the BTHS, which contributed to the positive temperature anomaly at surface (Fig. S2). Southerly winds facilitated the transportation of the aged air mass to north BTHS, contributing to the increased O₃ and its precursors. In addition to the local chemical formation and regional transportation of pollutants, deep sinking motion in the mid-lower troposphere and temperature inversion over the BTHS, which can restrain pollutant dispersion within a lower layer, also contributed to severe ozone pollution. Due to the inversion, ozone in the upper layer can be preserved at night because of the lack of NO titration. Once the inversion was broken as the sun rose the following day, ozone-rich air was vertically transported to the ground with the sinking motion, further aggravating the pollution. Because the abovementioned conditions remained in the BTHS, the heavy regional ozone pollution event could be continuously maintained.

Generally, high ozone pollution is accompanied by high UV radiation and temperature and a moderate RH at 30%–50%. In the BTHS and YRD, O₃ is positively correlated with temperature and UV radiation and negatively correlated with RH. Moreover, O₃ concentrations increase more significantly with a slope of 72.36 (μg/m³)/(MJ/m²) when UV radiation is greater than 2 MJ/m².

Conflict of Interest

The authors declare that they have no conflict of interest.

Acknowledgments

This work was supported by a grant from the National Key R&D Plan (Quantitative Relationship and Regulation Principle between Regional Oxidation Capacity of Atmospheric and Air Quality 2017YFC0210003), the National Natural Science Foundation of China (No. 41505133&41775162), and the National Research Program for Key Issues in Air Pollution Control (DQGG0101). We are grateful to the CMA and ECMWF for their data support.

Appendix A. Supplementary data

Supplementary data to this article can be found online at <https://doi.org/10.1016/j.jes.2020.02.019>.

REFERENCES

- Cheng, L., Wang, S., Gong, Z., Li, H., Yang, Q., Wang, Y., 2018. Regionalization based on spatial and seasonal variation in ground-level ozone concentrations across China. *Journal of Environmental Sciences* 67, 179–190.
- Cyrys, J., Pitz, M., Heinrich, J., Wichmann, H.E., Peters, A., 2008. Spatial and temporal variation of particle number concentration in Augsburg, Germany. *Sci. Total Environ.* 401 (1–3), 168–175.
- Ding, A.J., Fu, C.B., Yang, X.Q., Sun, J.N., Zheng, L.F., Xie, Y.N., et al., 2013. Ozone and fine particle in the western Yangtze River Delta: an overview of 1 yr data at the SORPES station. *Atmos. Chem. Phys.* 13 (11), 5813–5830.
- Fan, S., Wang, B., Tesche, M., Engelmann, R., Althausen, A., Liu, J., et al., 2008. Meteorological conditions and structures of atmospheric boundary layer in October 2004 over Pearl River Delta area. *Atmos. Environ.* 42 (25), 6174–6186.
- Farris, B.M., Gronoff, G.P., Carrion, W., Knepp, T., Pippin, M., Berkoff, T.A., 2019. Demonstration of an off-axis parabolic receiver for near-range retrieval of lidar ozone profiles. *Atmos. Meas. Tech.* 12 (1), 363–370.
- Ge, Q., Guo, X., Zheng, J., Hao, Z., 2008. Meiyu in the middle and lower reaches of the Yangtze River since 1736. *Chinese Sci. Bull.* 53 (1), 107–114.
- Gong, C., Liao, H., 2019. A typical weather pattern for ozone pollution events in North China. *Atmos. Chem. Phys.* 19 (22), 13725–13740.
- He, J., Wang, Y., Hao, J., Shen, L., Wang, L., 2012. Variations of surface O₃ in August at a rural site near Shanghai: influences from the West Pacific subtropical high and anthropogenic emissions. *Environ. Sci. Pollut. Res. Int.* 19 (9), 4016–4029.
- Krudysza, M.A., Froines, J.R., Fine, P.M., Sioutasc, C., 2008. Intra-community spatial variation of size-fractionated PM mass, OC, EC, and trace elements in the Long Beach, CA area. *Atmos. Environ.* 42, 5374–5389.
- Langford, A.O., Senff, C.J., Banta, R.M., Hardesty, R.M., Alvarez, R.J., Sandberg, S.P., et al., 2009. Regional and local background ozone in Houston during Texas Air Quality Study 2006. *J. Geophys. Res.* 114. D00F12.
- Li, K., Chen, L., Ying, F., White, S.J., Jang, C., Wu, X., et al., 2017. Meteorological and chemical impacts on ozone formation: A case study in Hangzhou, China. *Atmos. Res.* 196, 40–52.
- Li, K., Jacob, D.J., Liao, H., Shen, L., Zhang, Q., Bates, a.K.H., 2018. Anthropogenic drivers of 2013–2017 trends in summer. *PNAS* 116 (2), 422–427.
- Li, M., Yao, Y., Luo, D., Zhong, L., 2019. The Linkage of the Large-Scale Circulation Pattern to a Long-Lived Heatwave over Mideastern China in 2018. *Atmosphere* 10 (2), 89.
- Lin, W., Xu, X., Zhang, X., Tang, J., 2008. Contributions of pollutants from North China Plain to surface ozone at the Shangdianzi GAW Station. *Atmos. Chem. Phys.* 8, 5889–5898.
- Liu, J., Wang, L., Li, M., Liao, Z., Sun, Y., Song, T., et al., 2019a. Quantifying the impact of synoptic circulation patterns on ozone variability in northern China from April to October 2013–2017. *Atmos. Chem. Phys.* 19 (23), 14477–14492.
- Liu, N., Lin, W., Ma, J., Xu, W., Xu, X., 2019b. Seasonal variation in surface ozone and its regional characteristics at global atmosphere watch stations in China. *J. Environ. Sci.* 77, 291–302.
- Pu, X., Wang, T.J., Huang, X., Melas, D., Zanis, P., Papanastasiou, D.K., et al., 2017. Enhanced surface ozone during the heat wave of 2013 in Yangtze River Delta region, China. *Sci. Total Environ.* 603–604, 807–816.
- Sarnat, J.A., Moise, T., Shpund, J., Liu, Y., Pachon, J.E., Qasrawi, R., et al., 2010. Assessing the spatial and temporal variability of fine particulate matter components in Israeli, Jordanian, and Palestinian cities. *Atmos. Environ.* 44 (20), 2383–2392.
- Seinfeld, J.H., 1988. Ozone Air Quality Models. *JAPCA* 38 (5), 616–645.
- Shen, L., Mickley, L.J., Tai, A.P.K., 2015. Influence of synoptic patterns on surface ozone variability over the eastern United

- States from 1980 to 2012. *Atmos. Chem. Phys.* 15 (19), 10925–10938.
- Shi, C., Yuan, R., Wu, B., Meng, Y., Zhang, H., Zhang, H., et al., 2018. Meteorological conditions conducive to PM_{2.5} pollution in winter 2016/2017 in the Western Yangtze River Delta, China. *Sci. Total Environ.* 642, 1221–1232.
- Sousa, S., Martins, F., Alvimferraz, M., Pereira, M., 2007. Multiple linear regression and artificial neural networks based on principal components to predict ozone concentrations. *Environ. Model. Software* 22 (1), 97–103.
- Tan, Z., Lu, K., Jiang, M., Su, R., Dong, H., Zeng, L., et al., 2018. Exploring ozone pollution in Chengdu, southwestern China: A case study from radical chemistry to O₃-VOC-NO_x sensitivity. *Sci. Total Environ.* 636, 775–786.
- Tang, G., Li, X., Wang, X., Xin, J., 2010. Effects of Synoptic Type on Surface Ozone Pollution in Beijing. *Environ. Sci.* 31 (3), 573–578.
- Tang, G., Wang, Y., Li, X., Ji, D., Hsu, S., Gao, X., 2012. Spatial-temporal variations in surface ozone in Northern China as observed during 2009–2010 and possible implications for future air quality control strategies. *Atmos. Chem. Phys.* 12 (5), 2757–2776.
- Tu, J., Xia, Z.-G., Wang, H., Li, W., 2007. Temporal variations in surface ozone and its precursors and meteorological effects at an urban site in China. *Atmos. Res.* 85 (3–4), 310–337.
- Wang, L., Li, W., Sun, Y., Tao, M., Xin, J., Song, T., et al., 2018a. PM_{2.5} Characteristics and Regional Transport Contribution in Five Cities in Southern North China Plain, During 2013–2015. *Atmosphere* 9 (4), 157.
- Wang, T., Wei, X.L., Ding, A.J., Poon, C.N., Lam, K.S., Li, Y.S., et al., 2009. Increasing surface ozone concentrations in the background atmosphere of Southern China, 1994–2007. *Atmos. Chem. Phys.* 9 (16), 6217–6227.
- Wang, T., Xue, L., Brimblecombe, P., Lam, Y.F., Li, L., Zhang, L., 2017. Ozone pollution in China: A review of concentrations, meteorological influences, chemical precursors, and effects. *Sci. Total Environ.* 575, 1582–1596.
- Wang, Y., Du, H., Xu, Y., Lu, D., Wang, X., Guo, Z., 2018b. Temporal and spatial variation relationship and influence factors on surface urban heat island and ozone pollution in the Yangtze River Delta, China. *Sci. Total Environ.* 631–632, 921–933.
- Wang, Y., Hu, B., Ji, D., Liu, Z., Xin, J., Zhang, H., et al., 2014. Ozone weekend effects in the Beijing-Tianjin-Hebei metropolitan area, China. *Atmos. Chem. Phys.* 14, 2419–2429.
- Wang, Y., Hu, B., Tang, G., Ji, D., Zhang, H., Bai, J., et al., 2013. Characteristics of ozone and its precursors in Northern China: A comparative study of three sites. *Atmos. Res.* 132–133, 450–459.
- Wang, Y., McElroy, M., Munger, J., Hao, J., Ma, H., Nielsen, C., et al., 2008. Variations of O₃ and CO in summertime at a rural site near Beijing. *Atmos. Chem. Phys.* 8, 6355–6363.
- Whaley, C.H., Strong, K., Jones, D.B.A., Walker, T.W., Fogal, P.F., 2015. Toronto area ozone: Long-term measurements and modeled sources of poor air quality events. *J. Geophys. Res. Atmos.* 120 (21), 368–390.
- Wu, P., Ding, Y., Liu, Y., 2017. Atmospheric circulation and dynamic mechanism for persistent haze events in the Beijing–Tianjin–Hebei region. *Adv. Atmos. Sci.* 34 (4), 429–440.
- Xu, K., Lu, R., Mao, J., Chen, R., 2019. Circulation anomalies in the mid–high latitudes responsible for the extremely hot summer of 2018 over northeast Asia. *Atmos. Oceanic Sci. Lett.* 12 (4), 231–237.
- Xu, W., Zhao, C., Ran, L., Deng, Z., Liu, P., Ma, N., et al., 2011. Characteristics of pollutants and their correlation to meteorological conditions at a suburban site in the North China Plain. *Atmos. Chem. Phys.* 11, 4353–4369.
- Yan, X., Jianguo, L., Tianshu, Z., Guangqiang, F., Xinhui, S., Lihui, L., 2018. Differential absorption lidar combined with numerical model used for detecting distribution of ozone during summer in Hangzhou. *Optics Precis. Eng.* 26 (8), 1882–1887.
- You, Z., Zhu, Y., Jang, C., Wang, S., Gao, J., Lin, C.J., et al., 2017. Response surface modeling-based source contribution analysis and VOC emission control policy assessment in a typical ozone-polluted urban Shunde, China. *J. Environ. Sci.* 51, 294–304.
- Zhang, R., 2001. Relations of Water Vapor Transport from Indian Monsoon with That over East Asia and the Summer Rainfall in China. *Adv. Atmos. Sci.* 18 (5), 1005–1017.
- Zhang, Y.H., Su, H., Zhong, L.J., Cheng, Y.F., Zeng, L.M., Wang, X.S., et al., 2008. Regional ozone pollution and observation-based approach for analyzing ozone–precursor relationship during the PRIDE-PRD2004 campaign. *Atmos. Environ.* 42 (25), 6203–6218.
- Zhao, W., Tang, G., Yu, H., Yang, Y., Wang, Y., Wang, L., et al., 2019. Evolution of boundary layer ozone in Shijiazhuang, a suburban site on the North China plain. *J. Environ. Sci.* 83, 152–160.
- Zhao, Z., Wang, Y., 2017. Influence of the West Pacific subtropical high on surface ozone daily variability in summertime over eastern China. *Atmos. Environ.* 170, 197–204.
- Zheng, J., Zhong, L., Wang, T., Louie, P.K.K., Li, Z., 2010. Ground-level ozone in the Pearl River Delta region: Analysis of data from a recently established regional air quality monitoring network. *Atmos. Environ.* 44 (6), 814–823.
- Zhong, W., Yin, Z., Wang, H., 2019. The relationship between anticyclonic anomalies in northeastern Asia and severe haze in the Beijing–Tianjin–Hebei region. *Atmos. Chem. Phys.* 19 (9), 5941–5957.
- Zhu, J., Liang, X.-Z., 2012. Impacts of the Bermuda High on Regional Climate and Ozone over the United States. *J. Clim.* 26 (3), 1018–1032.